Formation of a metastable nanostructured mullite during Plasma Electrolytic Oxidation of aluminium in "soft" regime condition

J. Martin, A. Nomine, V. Ntomprougkidis, S. Migot, S. Bruyère, F. Soldera, T. Belmonte, G. Henrion

Materials and Design 180 (2019) 107977

Contents lists available at ScienceDirect

Materials and Design

journal homepage: www.elsevier.com/locate/matdes

Formation of a metastable nanostructured mullite during Plasma Electrolytic Oxidation of aluminium in "soft" regime condition

J. Martin [a,b,*], A. Nominé [a,c], V. Ntomprougkidis [a,b], S. Migot [a], S. Bruyère [a], F. Soldera [d], T. Belmonte [a], G. Henrion [a,b]

[a] Université de Lorraine, UMR 7198 CNRS, Institut Jean Lamour, Campus Artem, 2 allée André Guinier, F-54011 Nancy, France
[b] Laboratoire d'Excellence Design of Alloy Metals for low-mAss Structures ('LabEx DAMAS'), CNRS, Université de Lorraine, Ile du Saulcy, F-57045 Metz, France
[c] Department of Nanophotonics and Metamaterials, ITMO University, St. Petersburg 197101, Russia
[d] Department for Materials Science, Functional Materials, Saarland University, Saarbrücken D-66123, Germany

HIGHLIGHTS

- PEO in "soft" regime produces a 1:1 mullite/alumina lamellar nanocomposite
- The nanocomposite fills the "pancake" structure during the transition to "soft" regime
- Formation proceeds by a metastable solidification of a silicon-enriched alumina melt
- A better understanding of PEO coating formation in "soft"-regime is achieved.

GRAPHICAL ABSTRACT

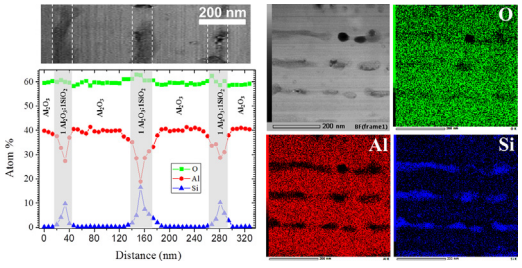

ARTICLE INFO

Article history:
Received 7 February 2019
Received in revised form 19 June 2019
Accepted 25 June 2019
Available online 27 June 2019

Keywords:
Plasma Electrolytic Oxidation (PEO)
Micro-arcs oxidation (MAO)
Aluminium
Mullite
Transmission electron microscopy (TEM)
Optical emission spectroscopy (OES)

Data availability:
The data that support the findings of this study are available from the corresponding author, JM, upon reasonable request.

ABSTRACT

This paper demonstrates the possibility of producing a lamellar ceramic nanocomposite at the top-most surface of oxide coatings grown with the Plasma Electrolytic Oxidation process (PEO). PEO was conducted on aluminium in a silicate-rich electrolyte under the so-called "soft" regime. Nanoscale characterisation showed that the transition from the "arcs" to the "soft" regime was concomitant with the gradual formation of a 1:1 mullite/alumina lamellar nanocomposite (≈120 nm thick) that filled the cavity of the PEO "pancake" structure. Combined with plasma diagnostic techniques, a three-step growth mechanism was proposed: (i) local melting of alumina under the PEO micro-discharges (≈3200 K at high heating rate $\approx 3 \times 10^8$ K·s^{-1}); (ii) progressive silicon enrichment of the melt coming from the electrolyte; and (iii) quenching of the melt at a cooling rate of $\approx 3.3 \times 10^7$ K·s^{-1} as the micro-discharge extinguishes. Under such severe cooling conditions, the solidification process was non-equilibrium as predicted by the metastable SiO_2 – Al_2O_3 binary phase diagram. This resulted in phase separation where pure alumina lamellae alternate periodically with 1:1 mullite lamellae.

1. Introduction

In a context of increasing demand in structure lightening, Al, Mg, Ti and their respective alloys are gaining a growing interest in various industrial domains, mainly the transport industry. However, their poor

* Corresponding author at: Université de Lorraine, UMR 7198 CNRS, Institut Jean Lamour, Campus Artem, 2 allée André Guinier, F-54011 Nancy, France.
E-mail address: julien.martin@univ-lorraine.fr (J. Martin).

https://doi.org/10.1016/j.matdes.2019.107977

surface performance in terms of wear and corrosion resistance still limits their use as critical parts in aeronautics or automotive industries. For decades, conventional anodising processes (acid or hard anodising) have been used to grow protective oxide ceramic coatings on Al, Mg and Ti based alloys. However, conventional anodising technology has reached some technical limits (*e.g.* low growth rate, limited thickness), and faces environmental and health issues because of the use of hazardous carcinogenic, mutagenic and reprotoxic (CMR) compounds (*e.g.* highly concentrated acids, borates, heavy metals, hexavalent chromium). To overcome these limitations, the Plasma Electrolytic Oxidation process (PEO) appears as a credible alternative to grow protective coatings on Al, Mg and Ti alloys [1–5]. Indeed, PEO is conducted in a diluted alkaline electrolyte (typically NaOH, KOH) free of hazardous compounds. In the case of aluminium, the resulting PEO layers exhibit improved hardness (1500 HV) and wear resistance (1×10^{-4} $mm^3 \cdot N^{-1} \cdot m^{-1}$) properties since the index of crystallinity of the grown aluminium oxide is close to 100%, compared with amorphous alumina in the case of conventional acid anodising. The PEO coatings on aluminium contain a significant proportion of high–temperature phases such as α-Al_2O_3 [6,7]. This is mainly due to the high temperature of non-equilibrium micro-discharges that develop over the processed surface. However, high energy consumption and lack of understanding of the interrelationships between processing conditions, discharge characteristics and resulting coating microstructure are the main restrictions for PEO coatings achieving a wider range of applications.

In this context, a pioneer work from Jaspard-Mécuson et al. [8] has shown that the suitable setting of the current waveform parameters promotes the appearance of a particular "soft" regime that occurs after a certain initial period of conventional PEO "arcs" regime. The "soft" regime is always associated with a gradual decrease in the electrical voltage, a lower intensity of the optical emission due to the gradual disappearance of micro discharges (MDs) and a reduction in the acoustic emission [8–10]. Despite the gradual disappearance of visible MDs during "soft" regime, advantages of PEO process are kept and some are even enhanced (*e.g.* higher growth rate, higher proportion of high temperature crystalline phases, lower porosity). The appearance of this "soft" regime is mainly promoted by the use of a bipolar current at the electrodes for which the ratio of positive to negative charge quantities (Q_p/Q_n) is lower than one, preferably in the range 0.8–1 [11]. Even in these conditions, the "soft" regime appears only after a delay that mainly depends on the current density and frequency [9,12]. On the other hand, the "arcs" regime designates either a treatment conducted with $Q_p/Q_n > 1$ or the period prior to "soft" regime for $Q_p/Q_n < 1$. Growing attention has been paid to this "soft" regime, even though only few MDs are visible. This regime is associated with an increase in growth rate and a reduction of the oxide layer porosity [13,14], while the process energy consumption is reduced by 20–30%. Nevertheless, the mechanisms that govern the transition from the detrimental "arcs" regime to the beneficial "soft" regime are not well understood yet. More specifically, the relationships that exist between the PEO processing conditions and the discharge mechanisms in the formation of the PEO coatings are still under debate [15–21].

Based on optical emission spectroscopy observations, Hussein et al. [15] and Jovovic et al. [16] proposed a PEO mechanism involving several types of discharges with different physical properties. As a continuation of these works, Cheng et al. [17–19] proposed the existence of "inner" discharges that would remain confined within the coating, in the open (unsealed) discharge channels (also called "pancake" structure). Therefore, these discharges would be invisible to an outside observer or to any optical sensor, but would affect the coating growth. In particular, they demonstrated that discharges occurring in the "pancake" cavity and referred to as D-type by Hussein et al. [15] and Cheng et al. [17–19] fill the cavity with a solidified material that contains a significant amount of electrolyte species, thus improving the wear resistance of the coatings. More recently, Rogov et al. [20,21] suggested that cathodic polarization could cause local acidification of the oxide/electrolyte interface (the electrical double layer (EDL)). This would result in a decrease in the EDL potential, an increase in the electrical conductivity of the coating under the subsequent anodic polarization and a decrease in the probability of discharge ignition. However, although these mechanisms describe some specific behaviours of the PEO process conducted in the "soft" regime conditions, the typical microstructure of the PEO coatings prepared within this particular "soft" regime conditions is still not accurately characterised at the sub-micrometer scale.

Though it is generally established that PEO processing of aluminium results in the formation of different crystallographic phases of aluminium oxide (mainly γ-, η- and α-Al_2O_3 in various proportions depending on the process conditions), some studies reported the additional presence of a 3:2 mullite phase ($3Al_2O_3.2SiO_2$) especially when using silicate-rich alkaline electrolytes [22–26]. Curran et al. [22] demonstrated that these mullite-based PEO coatings offer considerable promise as thermal barriers ($K \approx 0.5$ $W \cdot m^{-1} \cdot K^{-1}$) compared to pure alumina PEO coatings ($K \approx 2$ $W \cdot m^{-1} \cdot K^{-1}$). From a mechanical point of view, Kalkanci et al. [23] pointed out that mullite-based PEO coatings exhibit a low global stiffness (≈40 GPa) compared to pure alumina PEO coatings (≈170 GPa), which reduces the magnitude of thermally-induced stresses in the coating whose resistance to spallation during thermal cycling increases. Using glancing angle X-ray diffraction measurements, Dehnavi et al. [24–26] showed that this mullite phase was mainly localised at the top surface of the PEO coatings. Nevertheless, among these works, no study reported a detailed microstructural description of this specific PEO mullite phase that could give clues to understand the mechanism responsible for its growth and thus help optimising mullite-based PEO coatings for thermal-barrier applications.

Based on an experimental approach which combined material and optical characterisation, this present paper focuses on the formation of mullite-based PEO coatings grown on aluminium in a silicate-rich electrolyte within the "soft" regime conditions. The microstructure of the mullite-rich PEO coatings is described at atomic scale using high resolution transmission electron microscopy (HR-TEM). To complement, optical emission spectroscopy (OES) was carried out to analyse the light emitted by the micro-discharges to estimate the gas temperature that could explain phase transitions induced by the discharges. Finally, a mechanism is proposed for the formation of a metastable mullite during PEO of aluminium in the "soft"-regime condition using a silicate rich-electrolyte.

2. Experimental procedure

A 5 mm thick plate of Al2024 aluminium alloy (3.8–4.9 at.% Cu, 1.2–1.8 at.% Mg, 0.3–0.9 at.% Mn, balance Al) was cut into parallelepipedic samples with dimensions of 50 × 30 × 5 mm (working area of 38 cm^2). The samples were PEO processed in a solution of potassium hydroxide ($[KOH] = 1$ $g \cdot L^{-1} \cong 0.018$ $mol \cdot L^{-1}$) and anhydrous sodium silicate ($[Na_2SiO_3] = 1.65$ $g \cdot L^{-1} \cong 0.014$ $mol \cdot L^{-1}$) diluted in deionized water. The electrolyte temperature T_{elec} was maintained at 300 K using a cooling system. PEO treatments were conducted by applying a square bipolar current to the electrodes. The use of a current controlled power supply made it possible to optimally set and control the anodic and the cathodic current amplitude, and therefore to control the respective charge quantities delivered to the electrolyser system. In this work, the positive to negative charge quantities ratio (Q_p/Q_n) was kept at 0.9 in order to allow the occurrence of the "soft" regime [8–11]. The current frequency and the anodic current density were set at 500 Hz and 40 $A \cdot dm^{-2}$, respectively.

At the micrometer scale, the PEO oxide layers produced were observed by scanning electron microscopy (SEM) using a Phillips XL30 FEG instrument equipped with an EDX detector (TSL). For each processed sample, the top-most surface and the cross-section were examined using secondary electrons (SE; 5 kV accelerating voltage) and backscattered electrons (BSE; 25 kV accelerating voltage) detection modes. Cross-sections were prepared as follows: samples were cut, mounted in resin, polished with successive grades of *SiC* abrasive papers and polished

with a 1 μm diamond paste. Prior to SEM observations, the samples were coated with gold. For each sample, a minimum of 10 different SEM cross-section views were considered to determine an average coating thickness. The elemental composition of samples was determined by EDX measurements at different locations on the top-most surface of the coatings (25 kV accelerating voltage). Phase identification of the oxide layers was performed by X-ray diffraction (XRD) measurements using a Bruker D8 ADVANCE diffractometer (Cu-K_α incident radiation, $\lambda = 0.15056$ nm) operating in the θ/2θ Bragg-Brentano geometry with a step size of 0.02° over a scan range from 30 to 70°. The relative volume content of the α-Al_2O_3 phase with respect to the η-Al_2O_3 was deduced from XRD peak adjustments and calculated from the integrated intensity of α-Al_2O_3 peaks compared to the integrated ones of both α- and η- Al_2O_3 [27]. It must be mentioned here that, from a crystallographic point of view, γ- and η-Al_2O_3 belong to the same space group ($Fd\bar{3}m$) and exhibit the same lattice parameter (0.790 nm) making it difficult to discriminate each other by conventional XRD measurements conducted in θ/2θ Bragg-Brentano geometry. In the present study, in a better accordance with the JCPDS cards, the η- Al_2O_3 is suggested to be present in the produced PEO coating instead of the γ- Al_2O_3. Additionally, the phase characterisation of the top-most surface region of the oxide layers was carried out on an INEL CPS 120 diffractometer (Co-K_α incident radiation, $\lambda = 0.17903$ nm) operating in the grazing incidence X-ray diffraction geometry (GIXRD). GIXRD measurements were conducted with an incidence angle of 3° and the GIXRD patterns were recorded with a step size of 0.027° over the range 20–110°.

At the micro- and nanometre scales, the structure of the produced oxide layers was investigated by high-resolution transmission electron microscopy (HR-TEM). The specimen for HR-TEM was a cross-section slice of the oxide coating prepared by means of a focused ion beam (FIB) technique on a SEM dual beam facility (FEI Helios 600). The slice was extracted at an acceleration voltage of 30 kV and different ion currents. The last polishing step was done at 5 kV in order to reduce possible material amorphisation and defect formation. A JEOL ARM 200F – cold FEG UHR - transmission electron microscope operating at 200 kV and equipped with a Cs corrector was used for HR-TEM observations. In scanning mode (STEM), EDX analyses were obtained using a JEOL CENTURIO energy-dispersive X-ray spectrometer with a probe size of 1 nm. The quantification limit of the EDS detector is ±1 at.%. EDX element distribution maps recorded over an area of 512 nm × 512 nm (1 measurement point per nm) were produced by using an acquisition time of 1 ms per data point and by repeating 20 scans over the same area. In addition, an EDX line-scan profile consisting of 40 measurements points distributed over a line of 330 nm in length was also recorded with an acquisition time of 1 min per measurement point.

In addition, optical emission spectroscopy (OES) measurements were performed during the PEO process, using a 550 mm focal length monochromator (Jobin-Yvon TRIAX 550) equipped with a 1800 g/mm grating (resolution of 0.02 nm) and coupled to an ICCD detector. Optical emission spectra were recorded within the wavelength range 200–900 nm. To ensure that the maximum light intensity was collected and to avoid absorption of near-UV wavelength radiations by the glass window of the PEO treatment cell, an appropriate optical fibre connected to the entrance slit of the spectrometer was immersed in the electrolyte and located at 30 mm from the sample.

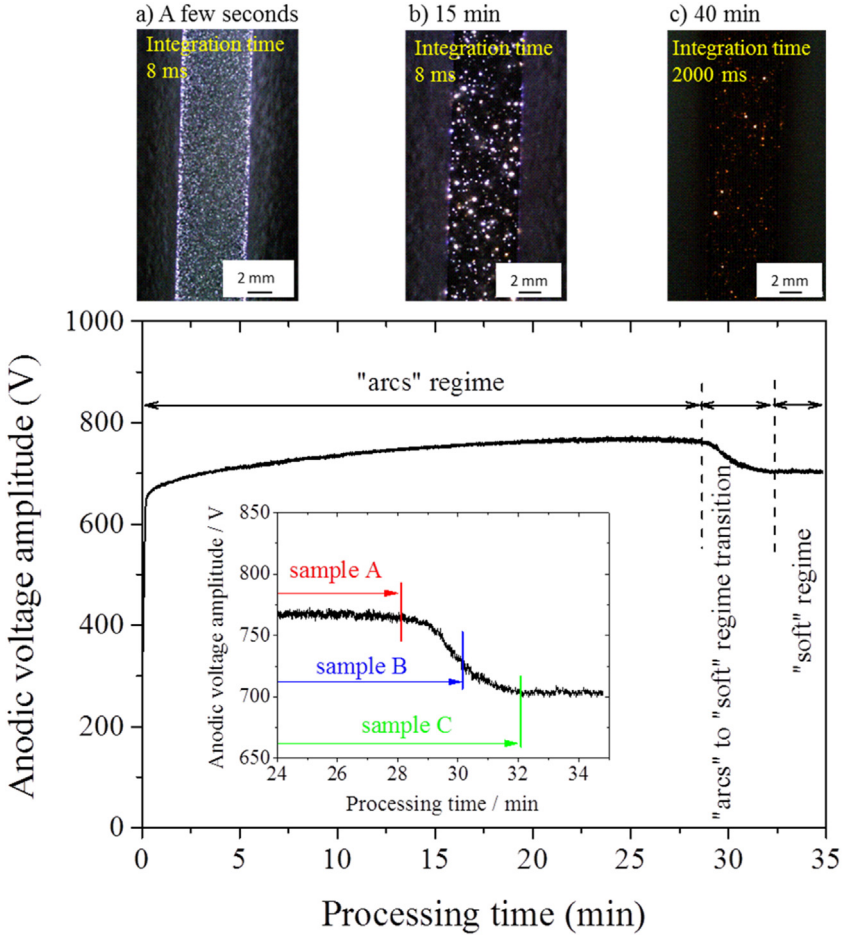

Fig. 1. Voltage-time response of an Al2024 aluminium alloy PEO processed within the "soft" regime electrical conditions ($Q_p/Q_n = 0.9$, F = 500 Hz, j = 40 A.dm^{-2}). Inset depicts the processing time of the samples A, B and C. Pictures recorded in similar PEO conditions illustrate the evolution of the micro-discharges aspects with time [8].

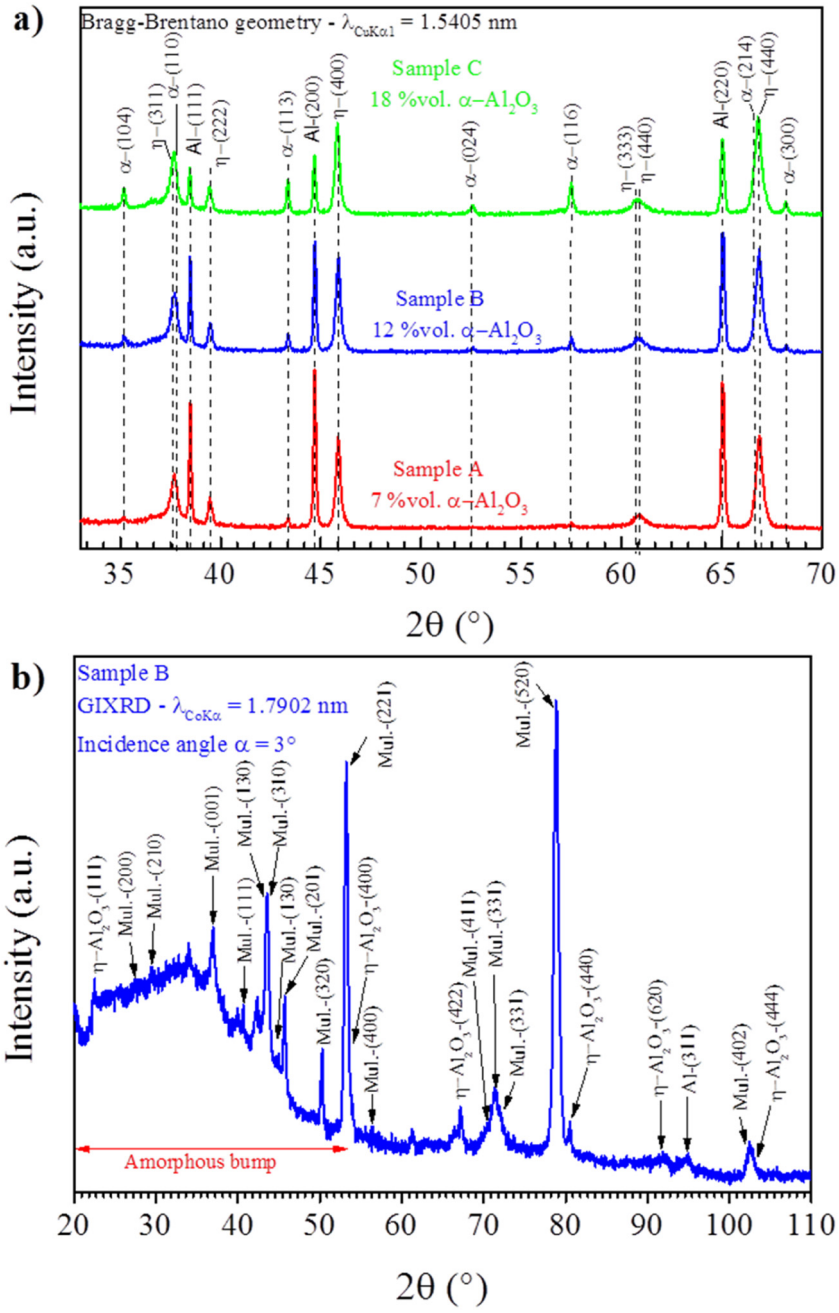

Fig. 2. a) XRD patterns of the processed samples with the calculated α-Al_2O_3 content (in vol%). and b) GIXRD pattern of the processed sample B. (Al for aluminium, α for α-Al_2O_3, η for η-Al_2O_3; Mul. for mullite).

3. Results

3.1. Voltage-time response

Fig. 1 shows the anodic voltage-time response of the system as a function of the PEO processing time. Four successive stages can be distinguished. During the first seconds, a barrier-type anodic film developed on the surface by conventional anodising mechanisms with a rapid increase in voltage amplitude (≈40 $V \cdot s^{-1}$). Then, the process suddenly entered in a discharge mode characterised by the appearance of white-orange discharges over the processed surface. During this "arcs" regime that ranged from 10 s to 28 min, the slope of the voltage-time curve reduced to 0.04 $V \cdot s^{-1}$. The third stage, ranging from 28 min to 32 min, corresponded to the "arcs" to "soft" regime transition, which was characterised by a gradual drop of the anodic voltage amplitude. This phenomenon is typical of bipolar PEO of aluminium conducted in "soft" regime conditions [8–11]. This voltage transition was directly correlated with a change of the optical and acoustic behaviour of the discharges that gradually turned to increasingly tiny discharges with shorter lifetimes, which limit the detrimental effects on the PEO layers [8,9]. Finally, the fourth regime ("soft" regime), was observed after 32 min of processing time. This ultimate regime had a constant and lower working voltage amplitude. Based on the voltage-time response presented in Fig. 1, three samples were processed differently. Sample A was processed till the end of the "arcs" regime (process stopped at 28 min). Sample B was processed until the "arcs" was changing to the "soft" regime (stopped at 30 min). Sample C was processed until the "soft" regime was fully established (stopped at 32 min).

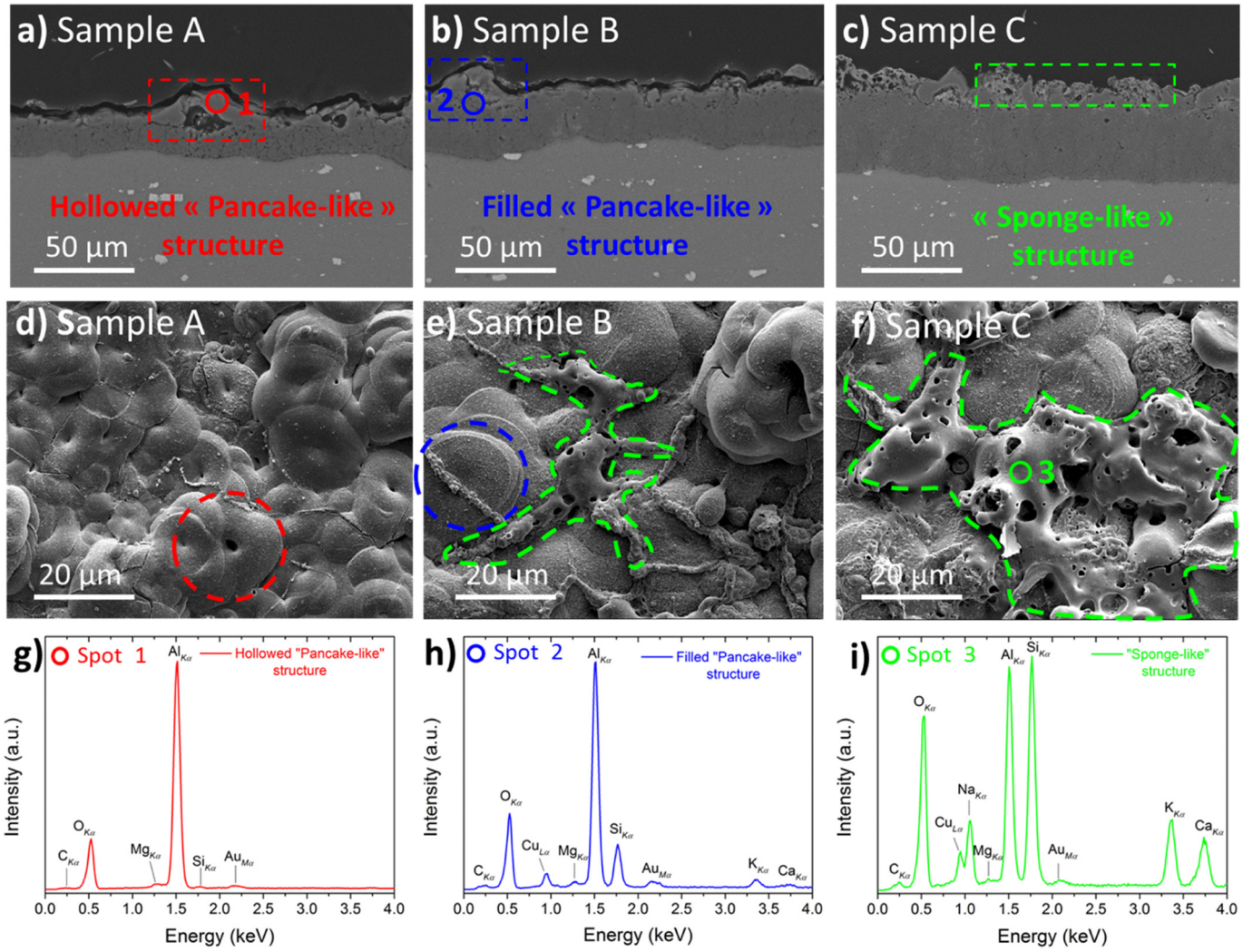

Fig. 3. SEM-BSE micrographs of the cross-sections (first row) and SEM-SE micrographs of the top-most surfaces (second row) of the samples processed: (a) and (d) just before the "soft" regime appearance (sample A), (b) and (e) transition of "arcs" to "soft" regime (sample B), (c) and (f) after the complete establishment of the "soft" regime (sample C). EDX spectra: (g) of the hollow "pancake"-like structure (red spot 1), (h) of the filled "pancake"-like structure (blue spot 2), and (i) of the "sponge"-like structure (green spot 3).

3.2. Multi-scale characterisation of the PEO oxide layers

Indexing the XRD patterns in Fig. 2a revealed that oxide coatings were composed of crystalline aluminium oxides α-Al_2O_3 (JCPDS card 00-010-0173) and η-Al_2O_3 (JCPDS card 01-077-0396) in various proportions. The transition to the "soft" regime was concomitant with the appearance of α-Al_2O_3 diffraction peaks whose intensity increased gradually as the "soft" regime proceeded. Indeed, just before the appearance of the "soft" regime (sample A), the coating was mainly composed of η-Al_2O_3 (7 ± 3 vol% α-Al_2O_3), while the one grown until the "soft" regime was completely established (sample C), exhibited the highest content of α-Al_2O_3 (18 ± 3 vol% α-Al_2O_3). This observation is in good agreement with previous studies which also showed a gradual enrichment in α-Al_2O_3 through the inner sublayer of the PEO coating when PEO process switched from the "arcs" to the "soft" regime [10,13]. The usual explanation considered the difference in the discharge behaviour before and after occurrence of the "soft" regime. In "arcs" regime (sample A), the B-type micro-discharges crossed the whole coating and therefore the major heat transfers occurred from the discharge to the substrate and the cooled electrolyte. Inversely, in the "soft" regime (sample C), the incomplete propagation of the inner D-type micro-discharges confined a significant part of heat within the coating rather than in the electrolyte, promoting the gradual transformation of the metastable η-Al_2O_3 into the thermodynamically stable α-Al_2O_3. The Al-peaks on the XRD patterns (JCPDS card 00-004-0787) were due to the scattering of the aluminium substrate under the oxide layer. When the "soft" regime started, the intensity of the Al-peaks started to decrease, suggesting that the oxide coating became thicker and more compact as the "soft" regime occurred. The grazing incidence XRD (GIXRD) pattern recorded on sample B is presented in Fig. 2b. The disappearance of Al-peaks on the GIRXD pattern in Fig. 2b confirmed that Al peaks detected on the XRD pattern in Fig. 2a originated from the substrate and showed that no crystalline aluminium existed in the PEO coating. In addition, the GIXRD pattern in Fig. 2b shows that the top-most surface of the grown oxide layer was composed of amorphous material and crystallised phases. These crystalline phases consisted of a mixture of alumina and mullite, the latter being a solid solution phase of η-Al_2O_3 (alumina) and SiO_2 (silica) in the Al_2O_3-SiO_2 binary system [28]. The presence of mullite in PEO coatings was reported by Dehnavi et al. [24–26] who also showed that the mullite phase was mainly located in the outer sublayer of the PEO coatings.

SEM micrographs of the cross-sections and the top-most surface of the processed samples are shown in Fig. 3. With the transition from "arcs" to "soft" regime, the morphology of the PEO coatings gradually transformed into a more compact and thicker oxide layer (26 ± 8 µm, 31 ± 5 µm, 55 ± 5 µm thick for samples A, B and C, respectively). For

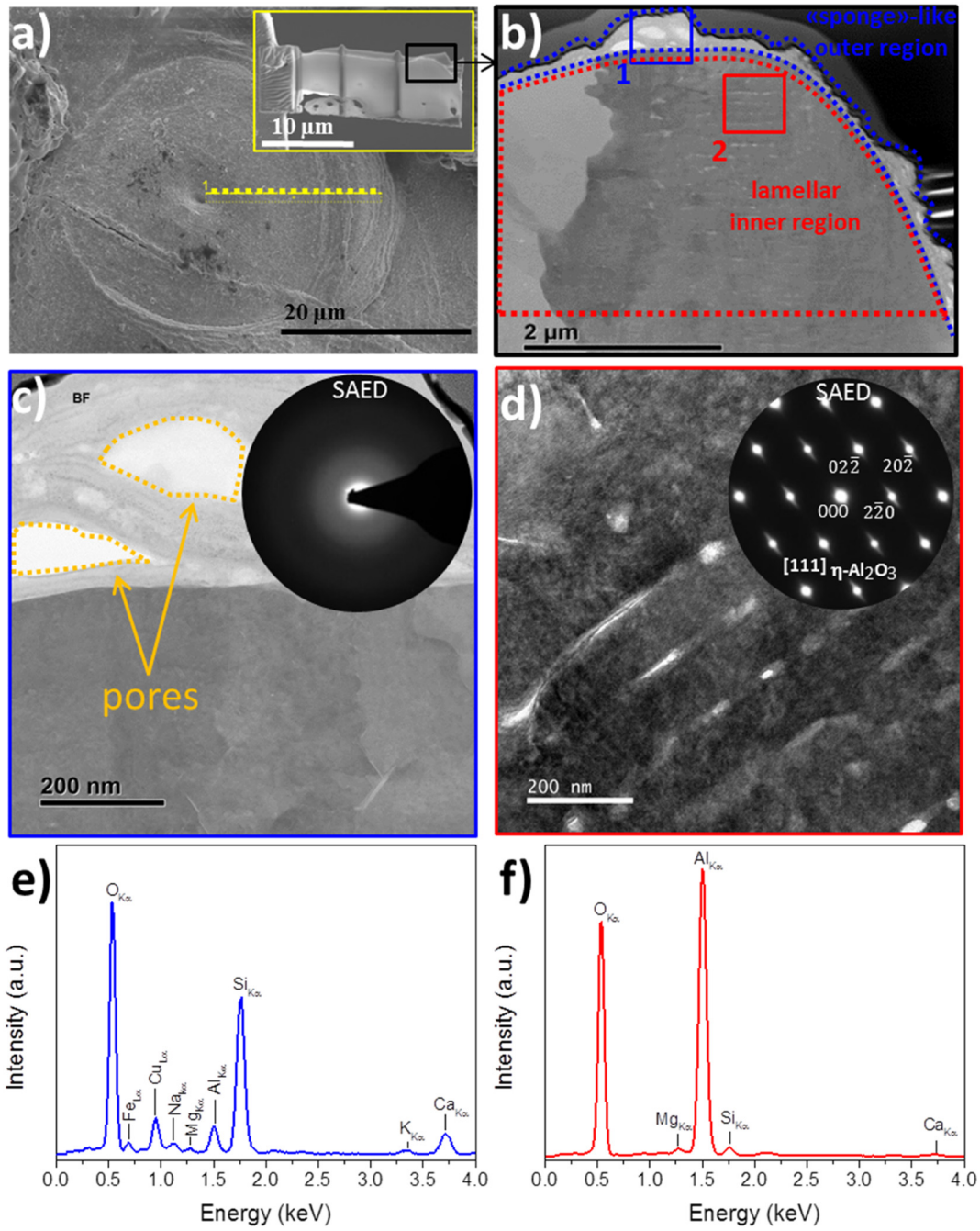

Fig. 4. (a) SEM-BSE micrograph of the top-most surface of the sample B. Dotted line shows the location of the extraction of the FIB foil cross-section. (b–d) Bright field STEM micrographs of the "pancake"-like structure and the associated SAED patterns. Integrated EDX spectra for: (e) outer porous sublayer located on the dome of the "pancake"-like structure (blue square) and (f) filled cavity of the "pancake"-like structure (red square).

sample A, processed before the occurrence of the "soft" regime (Fig. 3a and d), the morphology was characterised by large and unfilled oxide layer bulges. These bulges, commonly referred to as "pancake" structures [13], are typical of PEO coatings grown within the "arcs" regime and they are caused by strong electrical MDs. The EDX spectra recorded on the dome of a hollow "pancake" structure showed it mainly consisted of Al (≈31 at.%) and O (≈67 at.%) (Fig. 3g), which is consistent with the detection of alumina from GIXRD measurements (Fig. 2b). A small amount of Si (≈1 at.%) coming from the electrolyte was also detected while the presence of Au (≈1 at.%) was due to the gold sputtered coating of the surface prior to SEM observations. For sample B (Fig. 3b and e), collected during the transition from the "arcs" regime to "soft" regime, the cavity of the "pancake" structures was mainly filled with some solidified material. The EDX spectra recorded on this filler material showed it consisted mainly of Al (≈24 at.%) and O (≈63 at.%), but also Si (≈7 at.%), Ca (≈1 at.%), K (≈1 at.%), Na (≈1 at.%) Cu (≈1 at.%), Mg (≈1 at.%), and Au (≈1 at.%) (Fig. 3h). At the same time, the growth of an interconnected network of a "sponge"-like morphology was observed around and across "pancake" structures on the topmost surface of sample B (Fig. 3e). This "sponge"-like morphology, highly porous and with filaments, seemed to incorporate elements from both the electrolyte *e.g.* O (≈54 at.%), Si (≈13 at.%), Ca (≈5 at.%), K (≈2 at.%) and Na (≈1 at.%) and from the Al substrate *e.g.* Al (≈18 at.%), Cu (≈4 at.%) and Mg (≈2 at.%) (Fig. 3i). This observation is in good agreement with previous studies that showed that the formation of this "sponge"-like structure usually

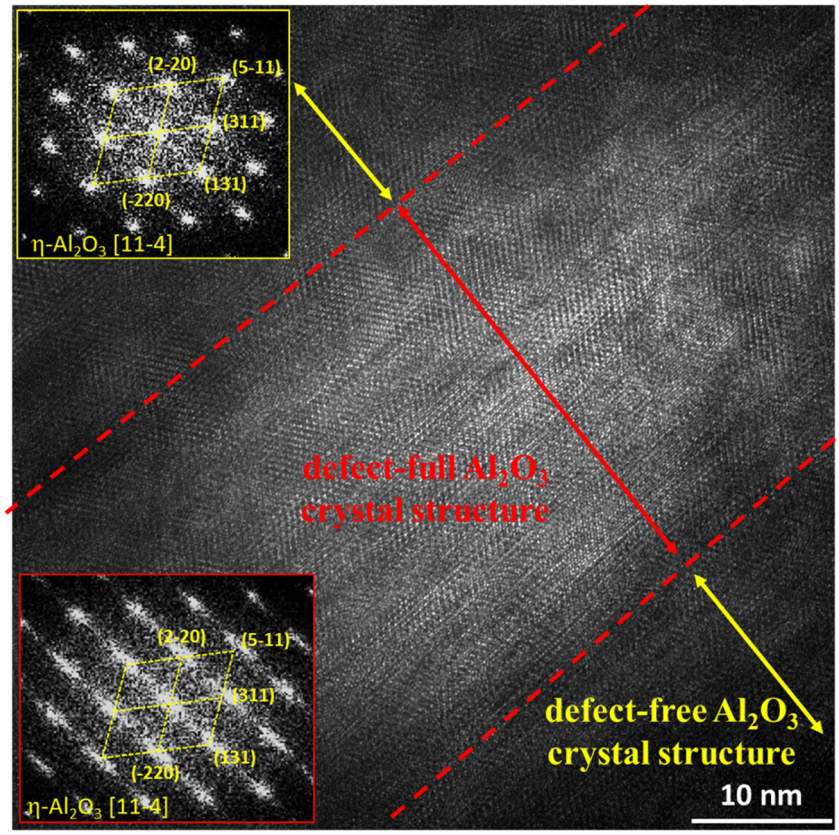

Fig. 5. High resolution TEM micrograph of the lamellar structure observed in the filled "pancake"-like structure of the processed sample B and the FFT patterns associated with the bright (red central region) and the dark lamellae (yellow lateral regions).

appears concomitantly with the transition to "soft" regime, whatever the processing conditions applied [9,10,13,29,30]. For sample C, when the "soft" regime was fully established (Fig. 3c and f), this "sponge" structure still continued to grow until it covered the entire surface of the sample as already reported [29,30]. Consequently, the previous "pancake" structure was progressively modified into a porous outer sublayer as the process went on. Although this "sponge" structure exhibits poor mechanical properties in terms of hardness and wear resistance due to its high porosity, several studies reported an interest in this porous outer sublayer. Particularly, some authors demonstrated that this "sponge" structure promoted the *in situ* incorporation of (nano-) particles from the electrolyte to the oxide layers, and can endow the PEO coatings with new functionalities such as hydrophobicity and biocompatibility [31–33]. The microstructure of sample B was thoroughly characterised at a sub-micrometer scale using TEM. For this, a thin slice of ≈60 nm in thickness was prepared from the surface using a FIB facility. This thin foil was vertically extracted through a filled "pancake" structure, as illustrated in Fig. 4a. The bright-field STEM (BF-STEM) micrograph in Fig. 4b shows two regions: a thin "sponge" like outer sublayer that seemed to cover the dome of the "pancake" structure (identified by blue dashed lines in Fig. 4b) and a thick denser inner sublayer (identified by red dashed lines in Fig. 4b). Indexing the selected area electron diffraction (SAED) pattern revealed that the "sponge"-like outer sublayer was completely amorphous (Fig. 4c). The EDX spectrum collected in this "sponge"-like region showed Si and O in large amounts (Fig. 4e), while other elements from the electrolyte (*e.g.* Na, K and Ca) and from the aluminium alloy substrate (*e.g.* Al, Cu, Mg and Fe) were in lower amounts. The formation of a thin Si-rich amorphous border on the top-most surface of the "pancake" structure was consistent with the detection of an amorphous phase with the GIXRD measurements (Fig. 2b). In contrast, indexing the SAED pattern recorded for the filled cavity of the "pancake" structure indicated the presence of the crystalline η-Al_2O_3 phase (Fig. 4d), suggesting that the crystalline α-Al_2O_3 phase, identified by XRD measurements (Fig. 2a), was located deeper in the PEO coating. This observation is in good agreement with experimental results by Tillous et al. [7] who showed from micro-focused X-ray synchrotron diffraction measurements that the α-Al_2O_3 phase was preferentially located under the "pancake" structures. These results were partly explained by Yerokhin et al. [34] who simulated the temperature field in a cylindric discharge channel by taking into account the heat dissipation into the adjacent oxide layer, the presence of the bulk Al substrate and the cooled electrolyte. With similar electrical conditions to those used here, they predicted that the η- to α-Al_2O_3 phase transition was more likely to occur in the internal sublayer than in the outer one, the latter being subject to a higher cooling rate. In addition, the SAED pattern in Fig. 4d also shows that each bright diffraction spot had a diffuse streak, suggesting the presence of defects in the η-alumina crystal structure. The BF-STEM micrograph of the filled cavity of the "pancake" structure revealed nanoscale lamellae (Fig. 4d). Bright and thin lamellae alternated periodically with dark and thick lamellae. The EDX spectrum in Fig. 4f, integrated over this lamellar arrangement, showed the presence of Al and O in large amounts and Si, Ca and Mg in lower amounts. Fig. 5 shows an HR-TEM micrograph of this lamellar structure and the associated FFT patterns recorded on both the bright and the dark lamellae. Indexing the FFT patterns confirmed crystallised η-alumina. However, the presence of long and diffuse streaks on the FFT pattern recorded on the bright lamellae clearly shows that η-alumina lamellae had numerous crystallographic defects, while dark lamellae were weakly-faulted crystals, confirmed by the presence of well-defined circular spots on the corresponding FFT pattern. For this particular lamellar arrangement, a closer examination of the element distribution was done with STEM/EDX analyses. The latter

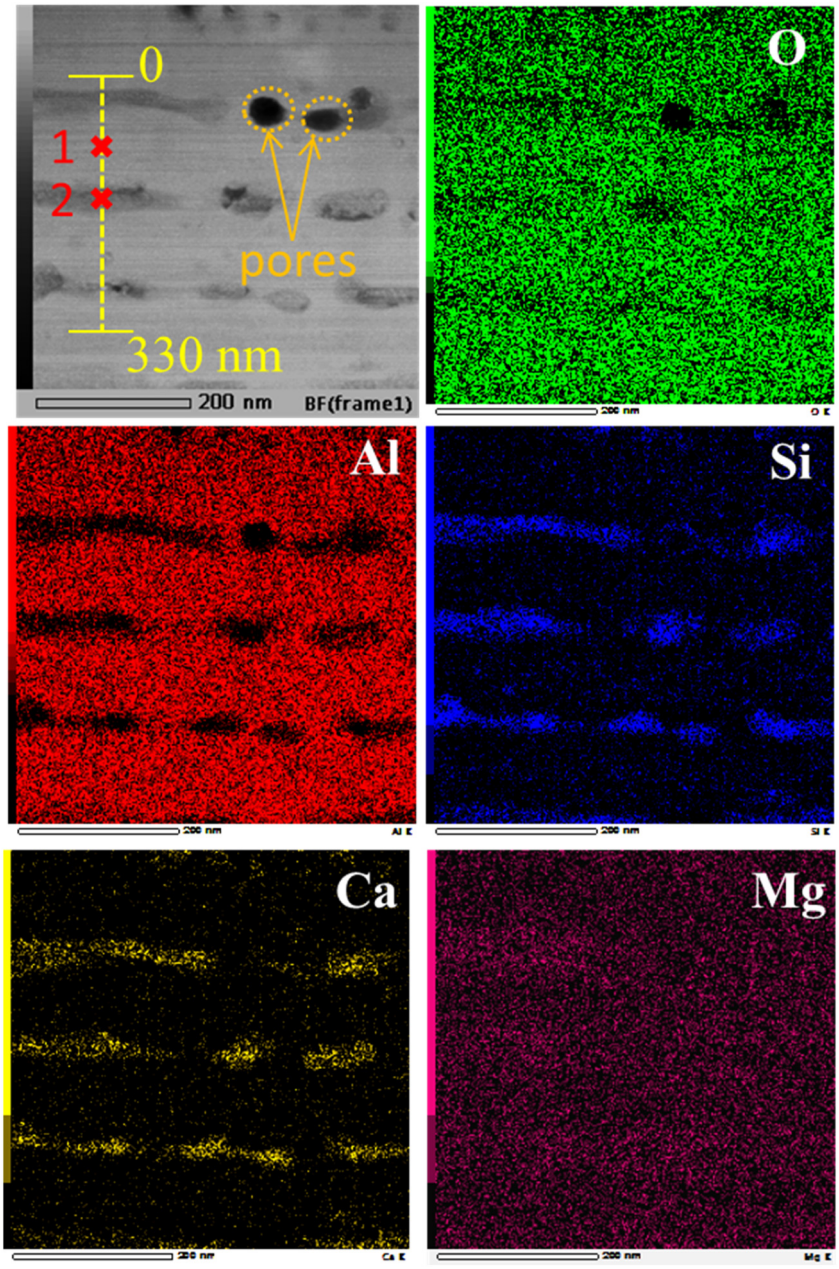

Fig. 6. Dark-field STEM (DF-STEM) micrograph recorded over a 500 nm × 500 nm square area in the filled "pancake"-like structure of the processed sample B and the associated STEM/EDX elemental maps.

were performed over a 500 nm × 500 nm square area as defined in the dark-field STEM (DF-STEM) micrograph in Fig. 6. The thin and faulted lamellae were enriched in Si, Ca and Mg, while the thick and weakly-faulted lamellae were depleted in these elements. The EDX spectrum given in Fig. 7a was recorded in the weakly-faulted alumina lamellae (spot #1 in Fig. 6). The associated amount in each element is also given in Fig. 7a. The presence of Mg, Si, and Ca can be neglected, since the their respective amount is in the same range as the quantification limit of the EDX detector (±1 at.%). Thus, weakly-faulted lamellae consisted mainly of O (59.7 at.%) and Al (39.3 at.%), close to stoichiometric Al_2O_3. In contrast, the EDX spectrum given in Fig. 7b and recorded in the faulted lamellae (spot #2 in Fig. 6) shows that they mainly contained O (62.8 at.%), Al (18.9 at.%) and Si (16.5 at.%). This result clearly suggests that the faulted lamellae likely consisted of the mullite phase as previously detected with GIXRD measurements in Fig. 2b. Indeed, the presence of stacking faults in the HR-TEM micrograph in Fig. 5 and the diffuse streaks on each electron diffraction spot in Fig. 4d can be attributed to the formation of the mullite phase. It can be explained by considering the η-alumina structure that consists of chains of AlO_6 octahedra cross-linked with chains of AlO_4 tetrahedra. When the mullite phase is forming, SiO_4 tetrahedra randomly replaced AlO_4 tetrahedra through the initial η-alumina structure, giving rise to structural defects and a distorted η-alumina structure [28]. From the STEM/EDX elemental line-scan defined on the DF-STEM micrograph in Fig. 6, the average periodicity of this lamellar nanocomposite structure was estimated at about 120 nm (Fig. 8). The average thickness of each type of lamella was determined at 30 nm for the thin and faulted Si-rich lamellae, and 90 nm for the thick and weakly-faulted Si-poor lamellae.

3.3. Optical characterisation of the micro-discharges (OES)

The accurate determination of the temperature inside the micro-discharges is needed in order to describe the microstructure formation

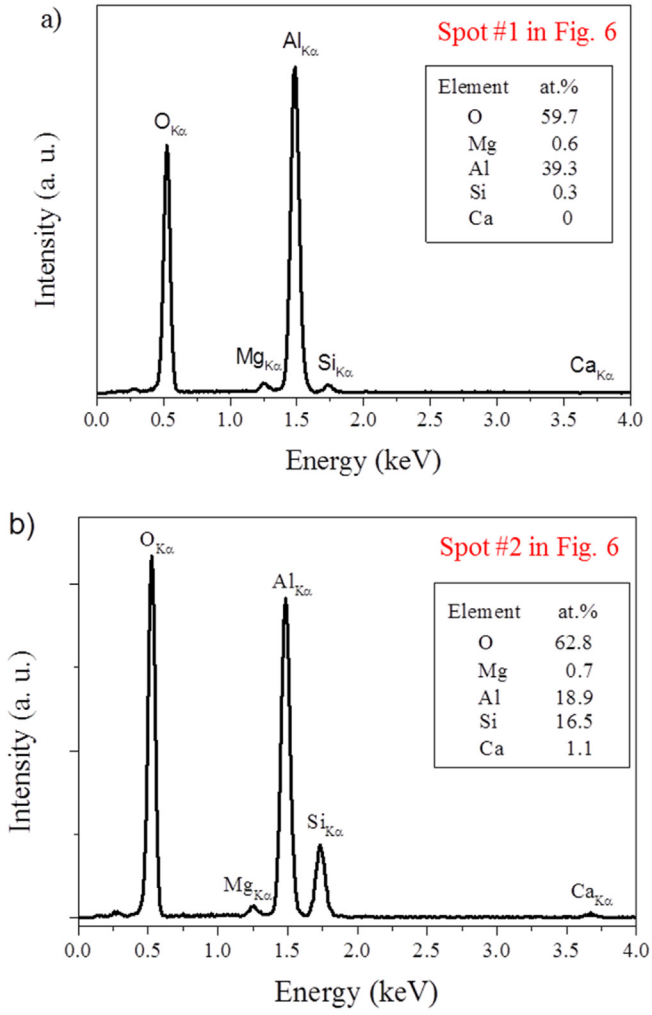

Fig. 7. EDX spectra and the associated element quantification recorded a) on the thick and defect-free lamellae (spot 1) and b) on the thin and defect-full alumina lamellae (spot 2). Locations of the spot #1 and the spot #2 are defined in the DF-STEM micrograph in Fig. 6.

during PEO. Its value can be estimated in part by conducting optical emission spectroscopy (OES) measurements as described by Bruggeman et al. [35,36] and Belmonte et al. [37]. Fig. 9 shows the OES spectrum recorded during the PEO processing of the aluminium alloy in a KOH/Na_2SiO_3-containing electrolyte. This spectrum was collected during the transition from the "arcs" to the "soft" regime. It shows emission lines of the electrolyte species (*e.g.* Na, H_α, H_β, K, OH, O) and some others from the aluminium alloy substrate (*e.g.* Al, Cu). Analysis of this spectrum allows determining the excitation temperature T_{exc} using the Boltzmann plot method [35–37]. This excitation temperature T_{exc} is similar to the electron temperature T_e, provided the plasma is in thermodynamic equilibrium, at least in local thermodynamic equilibrium (LTE). The latter can be reasonably assumed for PEO discharges that consist of arc discharges. However, depending on the emission lines that are used, different values of T_e can be obtained. For instance, Jovović et al. [16] estimated T_e to ≈4000 K from Mg emission lines, while during the same treatment T_e has been estimated at ≈33,000 K when using O^+ lines. This effect was observed in the present case where T_e determined from Al^+ lines was 10,000 K ± 2000 K, while the same determination using O^+ lines gave an average value of 40,000 K ± 10,000 K (Fig. 10). These two temperature values can be due either to the presence of two groups of discharges with different properties, or to discharges composed of two regions, a hot and dense core and a colder and less dense outer region. All OES measurements were integrated over the whole sample surface and over several periods of the applied current.

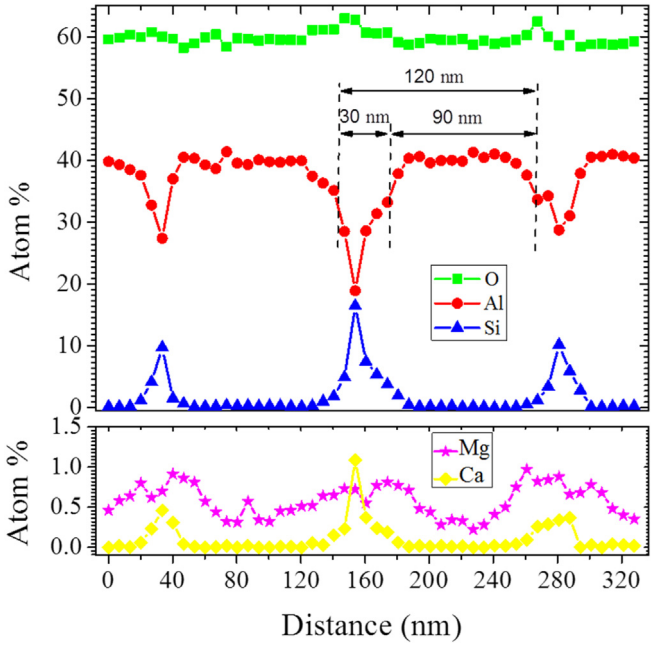

Fig. 8. STEM/EDX element line-scan profile through the lamellar nanocomposite morphology observed in the filled "pancake"-like structure. The location of the line-scan is defined in the DF-STEM micrograph in Fig. 6.

Therefore, reported T_e values were averaged values and the determination of two T_e values is still under debate in the PEO community. If T_e is usually considered as valuable information on the physical processes taking place within the plasma, it only characterises the electrons inside the plasma and reflects neither the gas, nor the surface temperature; it is therefore unsuitable to support the possibility of phase transitions in the solid in contact with the plasma.

However, in presence of molecules in the plasma, OES makes it possible to measure vibrational T_v and rotational T_r temperatures. Since rotational levels are very sensitive to Brownian motion, rotational temperature gives an excellent estimate of the gas temperature [38]. The OES spectrum during PEO processing of aluminium revealed only two molecular bands, corresponding to the transitions AlO ($B^2\Sigma^+$, v' = 0 ➔ A^2X^+, v = 0) at 484.2 nm and OH ($A^2\Sigma^+$, v' = 0 ➔ $X^2\Pi$, v = 0) at 306.8 nm. In the present study, the OH band was chosen because of the strong interference between H_β line and AlO band which would

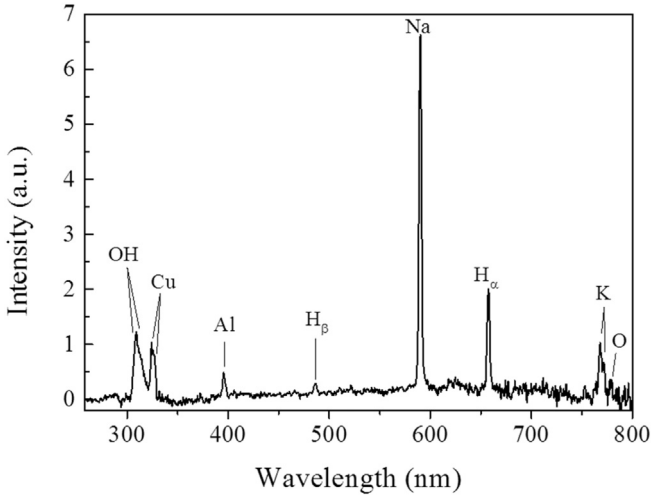

Fig. 9. Typical low resolution emission spectrum (260 nm–800 nm) of the micro-discharges recorded during PEO of aluminium (Al2024) in silicate-rich electrolyte.

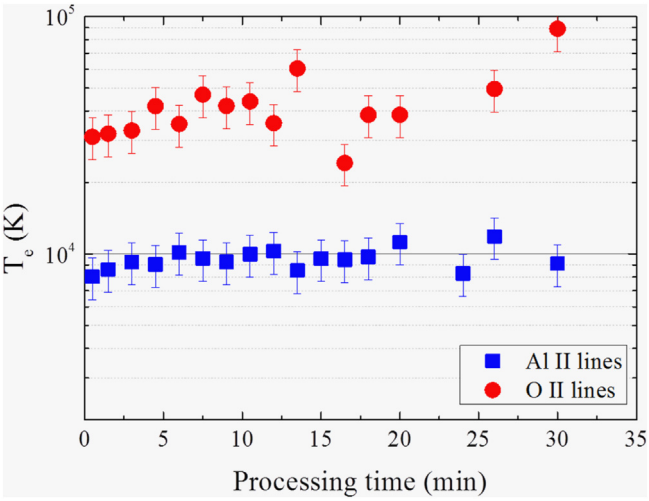

Fig. 10. Variation of the excitation temperature (assumed to be close to the electron temperature T_e) in the micro-discharges as a function of treatment time. Temperatures were estimated from the Boltzmann plots of the Al^+ lines (Al II) and the O^+ lines (O II).

have jeopardised the band profile fitting. The spectrum of the OH rotational bands given in Fig. 11 was fitted with the rotational temperature as a fitting parameter. The best fit was obtained for a temperature of 3200 K, which is consistent with that obtained by Stojadinovic et al. (3500–4000 K) [39,40].

4. Discussion

The discussion hereafter focuses on the description of a melting/solidification route to explain the formation of the 1:1 mullite/alumina lamellar nanostructure that gradually filled the "pancake" cavity during the PEO "soft" regime. Estimation of key parameters determining the development of such a nanostructure was needed first, as detailed in the following sections. Estimation of the heating rate *HR* experienced by the solidified material under the micro-discharges, estimation of the cooling rate (*CR*) experienced by the alumina-siliceous melt in contact with the cooled surrounding

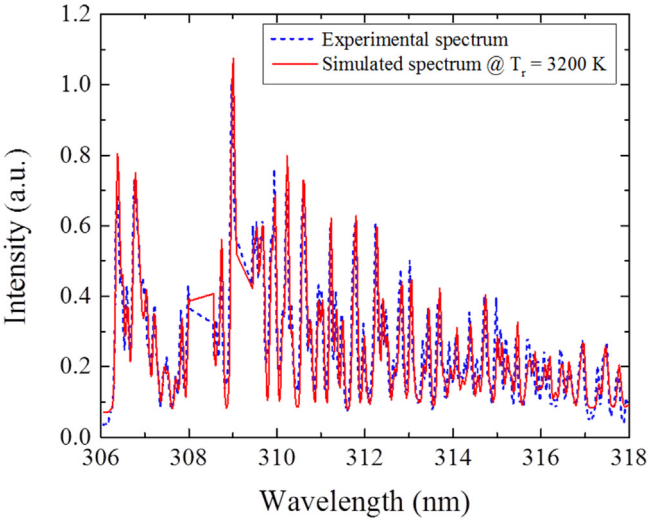

Fig. 11. Emission spectrum of the molecular OH ($A^2\Sigma^+$, v' = 0 → $X^2\Pi$, v = 0) band from the micro-discharges recorded during PEO of aluminium in silicate-rich electrolyte (dotted blue line). Simulated emission spectrum for a rotational temperature T_r = 3200 K (red line). Emission lines of Al (transition multiplet at 308,217 nm, 309.271 and 309,284 nm) were deliberately removed from the spectrum before applying the adjustment procedure.

electrolyte and estimation of the crystallisation temperature (T_c) at which the material solidification starts were successively conducted. These key thermodynamic parameters were estimated based on the combined results from the multi-scale characterisation of the "pancake" structure and from the optical characterisation of the micro-discharges. In addition, and as a first assumption, this interpretation was exclusively based on the phase transitions predicted by the SiO_2 - Al_2O_3 binary phase diagram [28] because Al, Si and O were the main elements detected in the lamellar nanocomposite, while Mg and Ca can be considered as negligible (Fig. 7).

4.1. Estimation of the heating rate (HR)

Estimation of the heating rate (*HR*) experienced by the solidified material under the micro-discharge was based on the optical emission spectroscopy results. As discussed above, the rotational temperature T_r of the OH molecules in the plasma of the micro-discharge can reasonably be assumed equal to the gas temperature T_{gas}, $T_{gas} \approx T_r \approx 3200$ K. This temperature was therefore a good estimate of the temperature the material experienced within the micro-discharge. Considering the SiO_2 - Al_2O_3 binary phase diagram reproduced in Fig. 12 [28], and no matter the SiO_2 fraction in Al_2O_3, the material is liquid at that temperature. Therefore, the PEO alumina coating, initially in a solid state at the electrolyte temperature $T_{elec} \approx 300$ K, is locally melted within the micro-discharge and reaches the gas temperature $T_{gas} \approx 3200$ K. Additionally, previous studies using ultra-fast video imaging established that the average lifetime of the micro-discharges, Δt_{MD}, is in the range of 10 μs [41–46]. Thus, the heating rate *HR* can be estimated as:

$$HR \cong \frac{\Delta T_{heat}}{\Delta t_{MD}} \tag{1}$$

where $\Delta T_{heat} \approx T_{gas} - T_{elec}$. Using the above values for T_{gas}, T_{elec} and Δt_{MD} gave $HR \approx 3 \times 10^8$ K·s^{-1}. This value was probably underestimated, since the high temperature reached in the micro-discharges did not hold over the entire MD lifetime. Indeed, Δt_{MD} includes the ignition and the extinction time during which the gas temperature was lower.

4.2. Estimation of the crystallisation temperature (T_c)

Estimation of the crystallisation temperature, T_c, at which the material solidification started was based on the nanoscale characterisation of the 1:1 mullite/alumina lamellar arrangement that filled the "pancake" structure.

First, the volume fraction of alumina lamellae, V_{Alum}, (accordingly $V_{Mul} = 1 - V_{Alum}$ is the volume fraction of 1:1 mullite lamellae) in the nanocomposite arrangement was estimated using HR-TEM image analysis according to the parallelepipedic shape of mullite identified in literature [47–49]. In the nanostructured region in Fig. 4d, a minimum of 10 different views (400 nm × 400 nm) were considered for the estimation of the surface fraction of alumina lamellae. Thus, V_{Alum} was in the range of 75 to 85 vol% (accordingly V_{Mul} is in the range of 15 to 25 vol%).From V_{Alum}, the weight fraction of the alumina lamellae W_{Alum} in the nanocomposite arrangement (where W_{Mul} is the weight fraction of the 1:1 mullite lamellae) was calculated according to:

$$W_{Alum} = \frac{\rho_{Al_2O_3} V_{Alum}}{\rho_{Al_2O_3} V_{Alum} + \rho_{1:1\ Mul} V_{Mul})} \tag{2}$$

where $\rho_{Al_2O_3} = 3.96$ g. cm^{-3} and $\rho_{1:1\ Mul} = 3.05$ g. cm^{-3} are the density of pure alumina and 1:1 mullite phases, respectively. Hence, W_{Alum} was estimated in the range of 79 to 88 wt%] (accordingly W_{Mul} is in the range of 12 to 21 wt%]). From W_{Alum}, the molar fraction of the alumina lamellae M_{Alum} in the nanocomposite arrangement (where M_{Mul} is the molar

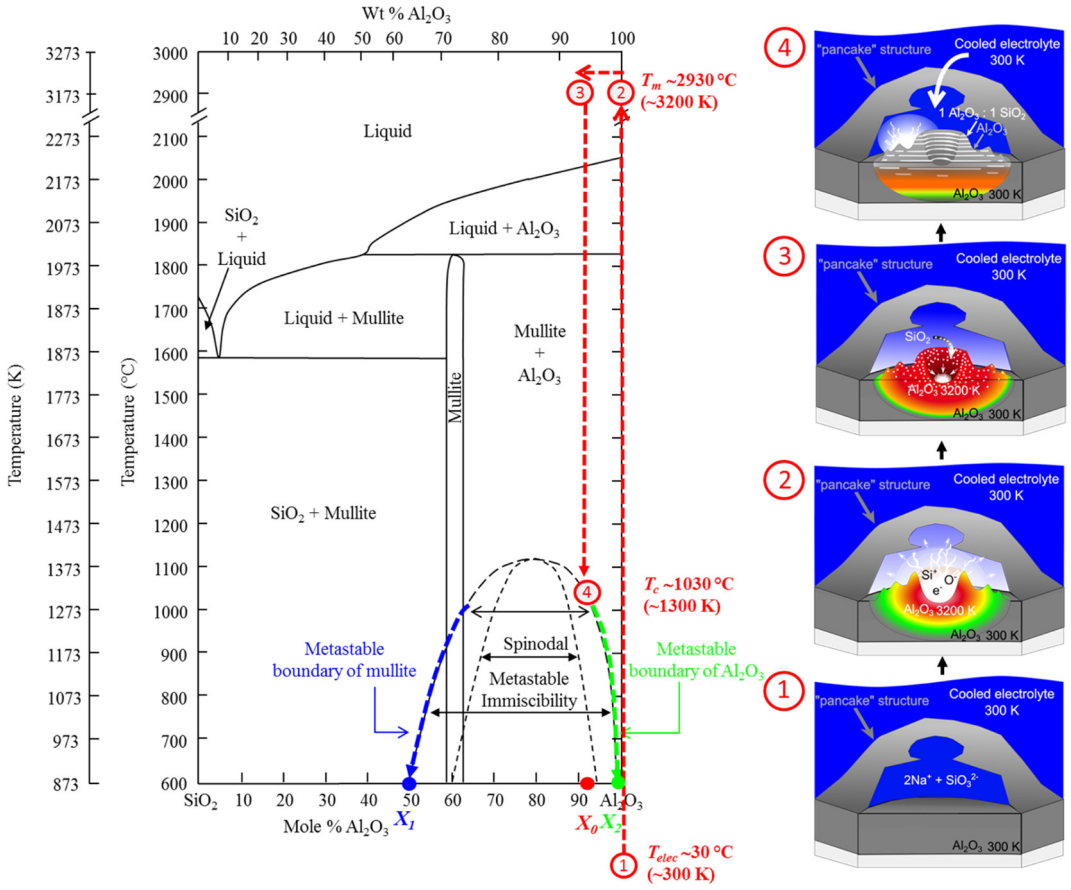

Fig. 12. Phase diagram for the Al_2O_3-SiO_2 binary system showing metastable regions in the mullite/Al_2O_3 domain and the proposed schematic representation of the formation of nanostructured metastable mullite in the pancake cavity during PEO of aluminium in "soft" regime condition [28]. 1: Arc discharging inside the pancake cavity that is associated with the propagation of a shock wave and the development of a spatial gradient of temperature from about 3200 K. 2: Melting of the pre-existing solidified alumina associated with the enrichment in Si. 3: Rapid quenching at about 3.3×10^7 K·s^{-1} due to the cooled surrounding electrolyte that filled the pancake cavity. 4: Mullite formation from a metastable phase transformation (solidification temperature at about 1300 K) and generation of new arc discharging which gradually leads to the filling of the pancake cavity.

fraction of the 1:1 mullite lamellae) was calculated using:

$$M_{Alum} = \frac{W_{Alum}/A_{Al_2O_3}}{W_{Alum}/A_{Al_2O_3} + (1-W_{Alum})/A_{1:1\ Mul}} \quad (3)$$

where $A_{Al_2O_3} = 101.96\,g \cdot mol^{-1}$ and $A_{1:1\ Mul} = 162.04\,g \cdot mol^{-1}$ are the molar weights of pure alumina and 1:1 mullite phases, respectively. Thus, M_{Alum} was estimated in the range of 86 to 92 mol% (accordingly M_{Mul} is in the range of 8 to 14 mol%).

Second, the amounts of O, Al and Si in the pure alumina lamellae were $C_{O/Alum} = 59.7$ *at.* %, $C_{Al/Alum} = 39.3$ *at.* % and $C_{Si/Alum} = 0.3$ *at.* %, respectively. The amount of Si was very low and lower than the accuracy of the EDX, about 1 at.%, so it was reasonable to assume that the alumina lamellae mainly consisted of pure crystallised Al_2O_3. Thus, using the SiO_2 - Al_2O_3 binary phase diagram [28], the molar fraction of Al_2O_3 in the alumina lamellae at room temperature (X_2 in Fig. 12) is 100 mol%. In contrast, EDX of the 1:1 mullite lamellae shows that the amounts of the O, Al and Si were $C_{O/Mul} = 62.8$ *at.* %, $C_{Al/Mul} = 18.9$ *at.* % and $C_{Si/Mul} = 16.5$ *at.* %, respectively. From the amount of Si in the mullite lamellae, the molar fraction of the Al_2O_3 phase in the mullite lamellae (X_1 in Fig. 12) was estimated at 50.47 *mol.* % following Eqs. (4)–(8). The amount of Si in mullite can be expressed as a function of the number of Si, Al and O atoms in the 1:1 mullite lamellae according to:

$$C_{Si/Mul} = \frac{N_{Si/Mul}}{N_{Si/Mul} + N_{Al/Mul} + N_{O/Mul}} \quad (4)$$

where $N_{Si/Mul}$, $N_{Al/Mul}$ and $N_{O/Mul}$ can be expressed as a function of the molar fraction of the Al_2O_3 phase in the mullite lamellae (X_1) and the Avogadro's number (noted $\mathcal{N}_A$):

$$N_{Si/Mul} = \frac{1}{3}(1-X_1)\mathcal{N}_A \quad (5)$$

$$N_{Al/Mul} = \frac{2}{5}X_1\mathcal{N}_A \quad (6)$$

$$N_{O/Mul} = \frac{2}{3}(1-X_1)\mathcal{N}_{A+}\frac{3}{5}X_1\mathcal{N}_A \quad (7)$$

X_1 was then determined from Eqs. (4)–(7):

$$X_1 = 1-3C_{Si/Mul} \quad (8)$$

Third, the nominal molar fraction of Al_2O_3 in the molten material at 3200 K (X_0 in Fig. 12) can be estimated from the lever rule:

$$M_{Alum} = \frac{X_0-X_1}{X_2-X_1} \quad (9)$$

Thus, X_0 was estimated in the range of 93 to 96 mol%.

Finally, by considering both the estimated molar fraction of Al_2O_3 in the nominal composition of the molten material and a metastable solidification route due to the high cooling rate experienced by the molten material (Section 4.3), the crystallisation temperature of the lamellar nanocomposite was estimated at about $T_c = 1300$ K. On the SiO_2 - Al_2O_3 binary phase diagram reproduced in Fig. 12 [28], this

crystallisation temperature corresponds to the boundary of the liquid miscibility gap between mullite and alumina at the nominal composition of the alumina-siliceous molten material.

4.3. Estimation of the cooling rate (CR)

The cooling rate, *CR*, experienced by the alumina-siliceous melt in contact with the cooled surrounding electrolyte required to form the metastable 1:1 mullite/alumina nanocomposite arrangement can be estimated according to:

$$CR \cong \frac{\Delta T_{cool}}{\tau_{Si}} \tag{10}$$

where $\Delta T_{cool} = T_c - T_{elec} = 1000$ K is the difference between the crystallisation temperature and the electrolyte temperature, and $\tau_{Si} \cong 3 \times 10^{-5}$ s is the diffusion time constant of Si in the solid Al_2O_3. τ_{Si} was calculated from the average diffusion length $\bar{\delta} \cong 60$ nm, measured from the STEM/EDX profile in Fig. 8:

$$\bar{\delta} = \sqrt{2.D_{Si/Al_2O_3}(T).\tau_{Si}} \tag{11}$$

where $D_{Si/Al_2O_3}(T) = 7 \times 10^{-11}$ m^2/s is the diffusion coefficient of Si in the Al_2O_3 phase at the metastable crystallisation temperature and at the corresponding estimated nominal composition X_0 between 93 and 96 mol% [50,51]. As suggested by Takamori et al. [50] and Chiang et al. [51], this diffusion coefficient can be calculated from the Stokes-Einstein equation:

$$D_{Si/Al_2O_3}(T) = \frac{kT}{6\pi r_{Si}\mu} \tag{12}$$

with $k = 1.38 \times 10^{-23}$ J.K^{-1} the Boltzmann constant, $\mu = 0.1$ Pa·s, the estimated dynamic viscosity at liquidus temperature for the nominal composition X_0 [52] and $r_{Si} = 1.36 \times 10^{-10}$ m the equivalent radius of Si estimated from:

$$r_{Si} = \frac{1}{2}\left(\frac{V_{M,Si}}{N_A}\right)^{1/3} \tag{13}$$

where $V_{M,Si} = 12 \times 10^{-6}$ m^3·mol^{-1} is the molar volume of Si, and $\mathcal{N}_A = 6.022 \times 10^{23}$ mol^{-1} the Avogadro's constant. Hence, the cooling rate was estimated at $C \approx 3.3 \times 10^7$ K·s^{-1}, which is in good agreement with the calculation of Yerokhin et al. (10^7 K·s^{-1}) [34].

4.4. Mechanism of melting/solidification route resulting in the lamellar nanocomposite

The mechanism proposed hereafter only focuses on the formation of the lamellar nanostructures observed inside the pancake cavity, and does not claim to be a full description of the growth mechanisms of PEO layers. Therefore, some precautions are needed and the discussion draws some assumptions. Firstly, it is assumed that the material transformations discussed here result from the ignition of a single micro-discharge. Hence, the combined effect of several micro-discharges that could appear at the same time in a close vicinity, especially the collective thermal effect, is not taken into account. For that, further studies are needed to introduce refinements of the proposed mechanism. Secondly, the discussion focuses on the exclusive presence of O, Al and Si elements that are distributed in various proportions through the 1:1 mullite/alumina lamellar nanocomposite. Indeed the amounts measured for Mg and Ca ($C_{Mg/Alum}$= 0.6 at.%, $C_{Mg/Mul}$= 0.7 at.%) and calcium ($C_{Ca/Alum}$= 0.0 at.%, $C_{Ca/Mul}$= 1.1 at.%) elements being within the detection limit of the STEM/EDX (1 at.%), the presence of Mg and Ca can be reasonably neglected. Consequently, the discussion is based on the SiO_2 - Al_2O_3 binary phase diagram that also shows metastable phases (Fig. 12) [28]. The schematic model in Fig. 12 illustrates the proposed mechanism of formation of the metastable 1:1 mullite/alumina lamellar nanocomposite observed into the cavity of the "pancake" structure.

First of all, although the electrical parameters fulfil the "soft" regime conditions, it is well established that the PEO process always starts conventionally with an "arcs" regime [10,13]. The PEO process gradually switches to the "soft" regime only after a certain processing time, usually after 10 to 30 min depending of the other process parameters. The "arcs" regime is characterised by visible and intense micro-discharges (mainly with strong B-type micro-discharges according to Hussein et al. [15]) which occur throughout the thickness of the PEO coating and induce large and unfilled discharge channels ("pancake" structure). In contrast, with the gradual appearance of the "soft" regime, visible and intense micro-discharges progressively change to tiny micro-discharges which develop inside the discharge channels that fill the "pancake" cavities. According to Cheng et al. [17–19] these tiny discharges are mainly of D-type. Consequently, with the appearance of the "soft" regime, the ignition of D-type discharges increasingly occurs inside the "pancake" cavity. With the ignition of a D-type micro-discharge, the solidified material that initially consisted of quite pure Al_2O_3 previously formed during the "arcs"-regime is locally and rapidly heated above $T_{gas} \approx 3200$ K with a heating rate of $HR \approx 3 \times 10^8$ K·s^{-1}. At this temperature, the pure alumina solid phase transforms into liquid. In addition, the elements present in the electrolyte can be more easily accepted into the coating through the surface discharging process. The SiO_3^{2-} anions present in the electrolyte enter the discharge channels through electrophoresis under the strong electric field, and undergo various excitation and dissociation processes in the micro-discharges. Dehnavi et al. [24–26] showed that SiO_3^{2-} anions dissociated into Si atoms in the plasma core. Klapkiv [53] described the transport in the channel of O and Si atoms from the core to the shell of the plasma due to temperature gradients. After about 10 μs, which is the average lifetime of the PEO micro-discharges in "soft" regime, the micro-discharge extinguishes and the plasma transport stops suddenly. The atomic species recombine to form gaseous O_2 and liquid SiO_2. Ultimately, just before the cooling step starts, the molten Al_2O_3 and the freshly formed SiO_2 combine in a liquid phase, resulting in an alumina-siliceous melt (Fig. 12). It is also worth noting that after one micro-discharge, it is expected that the melt is quite exclusively composed of alumina ($X_2 \approx 100$ mol. %). In turn, after repetitive ignition/extinction cycles of micro-discharges that are known to appear in successive bursts at the same location over the substrate [45], the alumina-siliceous melt is gradually enriched in SiO_2 and reaches the estimated nominal molar fraction of Al_2O_3 between 93 and 96 mol%.

As the micro-discharges extinguish, the pressure in the "pancake" cavity decreases and the cooled electrolyte enters into the open discharge channel. Consequently, the alumina-siliceous melt is quenched at cooling rate $CR \approx 3.3 \times 10^7$ K·s^{-1}. Within such severe cooling conditions, the solidification is expected to follow a non-equilibrium route as predicted by the SiO_2-Al_2O_3 phase diagram (Fig. 12) [28]. For a nominal molar fraction of Al_2O_3 in the range of 93 to 96 mol%, the solidification of the alumina-siliceous melt starts at the critical solidification temperature $T_c \approx 1300$ K as it is defined by the boundaries of the mullite/Al_2O_3 metastable immiscibility dome in Fig. 12. Therefore, a mechanism of phase separation takes place due to the precipitation of metastable mullite lamellae that alternate with metastable alumina lamellae. Close to the crystallisation temperature, the metastable mullite lamellae freshly formed are enriched in alumina (≈65 mol% Al_2O_3; ≈35 mol% SiO_2). Oppositely, the metastable alumina lamellae that are freshly formed are not 100% pure and contains a significant amount of SiO_2, up to 5 mol%. As the cooling process continues, and as predicted by the metastable branches of mullite and Al_2O_3 (blue-coloured and green-coloured in Fig. 12), the metastable mullite lamellae are progressively enriched in SiO_2 while the metastable alumina lamellae are gradually depleted in SiO_2 due to diffusion in the solid state [47–49]. At 870 K (limit of the phase diagram in Fig. 12 [28]), the alumina lamellae consists of Al_2O_3 ($X_2 \approx 100$ mol%), while the mullite lamellae contains about 50 mol% SiO_2 (50 mol% in Al_2O_3) that corresponds to the metastable 1:1 mullite. The molar fraction of the alumina lamellae M_{Alum} is also

higher (in the range of 86 to 92 mol%) than the molar fraction of the metastable 1:1 mullite M_{Mul} (in the range of 8 to 14 mol%). Finally, the microstructure predicted at 870 K by the proposed solidification mechanism remains close to the microstructure observed and characterised at room temperature in the present study.

5. Conclusions

A 2024 aluminium alloy was PEO processed in a KOH/Na_2SiO_3 electrolyte within the well-established "soft" regime electrical conditions. The microstructure of the "pancake" structure formed during the transition from the "arcs" regime to the "soft" regime was fully described. The cavity of the "pancake" structure was closely examined using high-resolution transmission electron microscopy. The main result showed that the beginning of the "soft"-regime was concomitant with the formation of a lamellar nanocomposite that gradually filled the cavity of "pancake" structure. This nanocomposite consisted of Al_2O_3 lamellae (≈90 nm in thickness) that periodically alternated with a metastable 1:1 mullite lamellae (≈30 nm in thickness). Combined with optical emission spectroscopy measurements performed during the transition to "soft" regime, a growth mechanism based on the metastable solidification route of a silicon-enriched alumina melt was proposed. Under the micro-discharge, alumina was locally melted above ≈3200 K at a high heating rate $\approx 3 \times 10^8\ K \cdot s^{-1}$. It was then gradually enriched in silicon due to the electrolyte decomposition and then cooled by the electrolyte at a high cooling rate $\approx 3.3 \times 10^7\ K \cdot s^{-1}$ after the micro-discharge extinction. Within such severe cooling conditions, the solidification process followed a non-equilibrium route as predicted by the metastable $SiO_2 - Al_2O_3$ phase diagram. It resulted in a phase separation consisting in a nanoscale lamellar arrangement of pure alumina (≈90 nm thick) and 1:1 mullite lamellae (≈30 nm thick).

CRediT authorship contribution statement

J. Martin: Supervision, Validation, Conceptualization, Investigation, Writing - original draft, Writing - review & editing. **A. Nominé:** Supervision, Validation, Conceptualization, Investigation, Writing - original draft, Writing - review & editing. **V. Ntomprougkidis:** Conceptualization, Investigation, Writing - review & editing. **S. Migot:** Investigation, Writing - review & editing. **S. Bruyère:** Investigation, Writing - review & editing. **F. Soldera:** Investigation, Writing - review & editing. **T. Belmonte:** Supervision, Validation, Writing - review & editing. **G. Henrion:** Supervision, Validation, Writing - review & editing.

Declaration of Competing Interest

The authors declare no competing financial interests.

Acknowledgements

- We greatly acknowledge the Conseil Regional de Lorraine for granting A. Nomine's PhD work under decision 11CP-769.
- This work was carried out as part of the COST TD1208 network.
- This work was supported by the French Government through the program "Investissements d'avenir" operated by the French National Research Agency (ANR) and referred to as ANR-11-LABX-0008-01 (LabEx DAMAS).
- The authors are grateful to Dr.-Ing. P. Boulet (Institut Jean Lamour, CC X-Gamma) for XRD measurements and Prof. N. St J. Braithwaite for fruitful discussions.

References

[1] A.L. Yerokhin, X. Nie, A. Leyland, A. Matthews, S.J. Dowey, Plasma electrolysis for surface engineering, Surf. Coat. Technol. 122 (1999) 73–93.

[2] Gh. Barati Darband, M. Aliofkhazraei, P. Hamghalam, N. Valizade, Plasma electrolytic oxidation of magnesium and its alloys: mechanism, properties and applications, J. Magnes. Alloy 5 (2017) 74–132.

[3] M. Toorani, M. Aliofkhazraei, Review of electrochemical properties of hybrid coating systems on mg with plasma electrolytic oxidation process as pretreatment, Surf. Interface 14 (2019) 262–295.

[4] Y. Cheng, T. Wang, S. Li, Y. Cheng, J. Cao, H. Xie, The effects of anion deposition and negative pulse on the behaviours of plasma electrolytic oxidation (PEO) – a systematic study of the PEO of a Zirlo alloy in aluminate electrolytes, Electrochim. Acta 225 (2017) 47–68.

[5] A. Mathis, E. Rocca, D. Veys-Renaux, J. Tardelli, Electrochemical behaviour of titanium in KOH at high potential, Electrochim. Acta 202 (2016) 253–261.

[6] L.R. Krishna, A.S. Purnima, G. Sundararajan, A comparative study of tribological behavior of microarc oxidation and hard-anodized coatings, Wear 261 (2006) 1095–1101.

[7] K. Tillous, T. Toll-Duchanoy, E. Bauer-Grosse, L. Hericher, G. Geandier, Microstructure and phase composition of microarc oxidation surface layers formed on aluminium and its alloys 2214-T6 and 7050-T74, Surf. Coat. Technol. 203 (2009) 2969–2973.

[8] F. Jaspard-Mecuson, T. Czerwiec, G. Henrion, T. Belmonte, L. Dujardin, A. Viola, J. Beauvir, Tailored aluminium oxide layers by bipolar current adjustment in the Plasma Electrolytic Oxidation (PEO) process, Surf. Coat. Technol. 201 (2007) 8677–8682.

[9] J. Martin, A. Melhem, I. Shchedrina, T. Duchanoy, A. Nominé, G. Henrion, T. Czerwiec, T. Belmonte, Effects of electrical parameters on plasma electrolytic oxidation of aluminium, Surf. Coat. Technol. 221 (2013) 70–76.

[10] T.W. Clyne, S.C. Troughton, A review of recent work on discharge characteristics during plasma electrolytic oxidation of various metals, Int. Mater. Rev. 64 (2019) 127–162.

[11] J. Martin, A. Nominé, F. Brochard, J.-L. Briançon, C. Noël, T. Belmonte, T. Czerwiec, G. Henrion, Delay in micro-discharges appearance during PEO of Al: evidence of a mechanism of charge accumulation at the electrolyte/oxide interface, Appl. Surf. Sci. 410 (2017) 29–41.

[12] F. Tjiang, L.W. Ye, Y.J. huang, C.C. Chou, D.S. Tsai, Effect of processing parameters on soft regime behavior of plasma electrolytic oxidation of magnesium, Ceram. Int. 43 (2017) S567–S572.

[13] D.S. Tsai, C.C. Chou, Review of the soft sparking regime issues in plasma electrolytic oxidation, Metals 8 (2018) 105.

[14] D.S. Tsai, G.W. Chen, C.C. Chou, Probe the micro arc softening phenomenon with pulse transient analysis in plasma electrolytic oxidation, Surf. Coat. Technol. 357 (2019) 235–243.

[15] R.O. Hussein, X. Nie, D.O. Northwood, A. Yerokhin, A. Matthews, Spectroscopic study of electrolytic plasma and discharging behaviour during the plasma electrolytic oxidation (PEO) process, J. Phys. D. Appl. Phys. 43 (2010), 105203.

[16] J. Jovovic, S. Stojadinovic, N.M. Sisovic, N. Konjevic, Spectroscopic study of plasma during electrolytic oxidation of magnesium- and aluminium-alloy, J. Quant. Spectrosc. Radiat. Transf. 113 (2012) 1928–1937.

[17] Y.L. Cheng, Z.G. Xue, Q. Wang, X.Q. Wu, E. Matykina, P. Skeldon, G.E. Thompson, New findings on properties of plasma electrolytic oxidation coatings from study of an Al–Cu–Li alloy, Electrochim. Acta 107 (2013) 358–378.

[18] Y.L. Cheng, J. Cao, Z. Peng, Q. Wang, E. Matykina, P. Skeldon, G.E. Thompson, Wear resistant coatings formed on Zircaloy-2 by plasma electrolytic oxidation in sodium aluminate electrolytes, Electrochim. Acta 116 (2014) 453–466.

[19] Y.L. Cheng, J. Cao, M. Mao, H. Xie, P. Skeldon, Key factors determining the development of two morphologies of plasma electrolytic coatings on an Al-Cu-Li alloy in aluminate electrolytes, Surf. Coat. Technol. 291 (2016) 239–249.

[20] A.B. Rogov, V.R. Shayapov, The role of cathodic current in PEO of aluminium: influence of cationic electrolyte composition on the transient current-voltage curves and the discharge optical emission spectra, Appl. Surf. Sci. 394 (2017) 323–332.

[21] A.B. Rogov, A. Yerokhin, A. Matthews, The role of cathodic current in Plasma Electrolytic Oxidation of aluminium: phenomenological concepts of the "soft sparking" mode, Langmuir 33 (2017) 11059–11069.

[22] J.A. Curran, H. Kalkanci, Y. Magurova, T.W. Clyne, Mullite-rich plasma electrolytic oxide caotings for thermal barrier applications, Surf. Coat. Technol. 201 (2007) 8683–8687.

[23] H. Kalkanci, S.C. Kurnaz, The effect of process parameters on mullite-based plasma electrolytic oxide coatings, Surf. Coat. Technol. 203 (2008) 15–22.

[24] V. Dehnavi, B.L. Luan, D.W. Shoesmith, X.Y. Liu, S. Rohani, Effect of duty cycle and applied current frequency on plasma electrolytic oxidation (PEO) coating growth behaviour, Surf. Coat. Technol. 226 (2013) 100–107.

[25] V. Dehnavi, X.Y. Liu, B.L. Luan, D.W. Shoesmith, S. Rohani, Phase transformation in plasma electrolytic oxidation on 6061 aluminium alloy, Surf. Coat. Technol. 251 (2014) 106–114.

[26] V. Dehnavi, B.L. Luan, X.Y. Liu, D.W. Shoesmith, S. Rohani, Correlation between plasma electrolytic oxidation treatment stages and coating microstructure on aluminium under unipolar pulsed DC mode, Surf. Coat. Technol. 269 (2015) 91–99.

[27] J. Martin, P. Leone, A. Nominé, D. Veys-Renaux, G. Henrion, T. Belmonte, Influence of electrolyte ageing on the Plasma Electrolytic Oxidation of aluminium, Surf. Coat. Technol. 269 (2015) 36–46.

[28] D.J. Duval, S.H. Risbud, J.F. Shackelford, Mullite, in: J.F. Shackelford, R.H. Doremus (Eds.), Ceramic and Glass Materials: Structure, Properties and Processing, Springer US, New-York, NY 2008, pp. 41–48.

[29] E. Matykina, R. Arrabal, P. Skeldon, G.E. Thompson, Investigation of the growth processes of coatings formed by AC plasma electrolytic oxidation of aluminium, Electrochim. Acta 54 (2009) 6767–6778.

[30] W. Gebarowski, S. Pietrzyk, Growth characteristics of the oxide layer on aluminium in the process of plasma electrolytic oxidation, Arch. Metall. Mater. 59 (2014) 407–411.
[31] X. Lu, M. Mohedano, C. Blawert, E. Matykina, R. Arrabal, K.U. Kainer, M. Zheludkevich, Plasma electrolytic oxidation coatings with particle additions – a review, Surf. Coat. Technol. 307 (2016) 1165–1182.
[32] E. Matykina, R. Arrabal, B. Mingo, M. Mohedano, A. Pardo, M.C. Merino, In vitro corrosion performance of PEO coated Ti and Ti6Al4V used for dental and orthopaedic implants, Surf. Coat. Technol. 307 (2016) 1255–1264.
[33] W.K. Yeung, I.V. Sukhorukova, D.V. Shtansky, E.A. Levashov, I.Y. Zhitnyak, N.A. Gloushankova, P.V. Kiryukhantsev-Korneev, M.I. Petrzhik, A. Matthewsa, A. Yerokhin, RSC Adv. 6 (2016) 12688–12698.
[34] A.L. Yerokhin, L.O. Snizhko, N.L. Gurevina, A. Leyland, A. Pilkington, A. Matthews, Discharge characterization in plasma electrolytic oxidation of aluminium, J. Phys. D. Appl. Phys. 36 (2003) 2110–2120.
[35] P. Bruggeman, D. Schram, M.A. Gonzalez, R. Rego, M.G. Kong, C. Leys, Characterization of a direct dc-excited discharge in water by optical emission spectroscopy, Plasma Sources Sci. Technol. 18 (2009), 025017.
[36] P. Bruggeman, T. Verreycken, M.A. Gonzalez, J.L. Walsh, M.G. Kong, C. Leys, D.C. Schram, Optical emission spectroscopy as a diagnostic for plasmas in liquids: opportunities and pitfalls, J. Phys. D. Appl. Phys. 43 (2010), 124005.
[37] T. Belmonte, C. Noel, T. Gries, J. Martin, G. Henrion, Theoretical background of optical emission spectroscopy for analysis of atmospheric pressure plasmas, Plasma Sources Sci. Technol. 24 (2015), 064003.
[38] P.J. Bruggeman, N. Sadeghi, D.C. Schram, V. Linss, Gas temperature determination from rotational lines in non-equilibrium plasmas: a review, Plasma Sources Sci. Technol. 23 (2014), 023001.
[39] S. Stojadinović, J. Jovović, M. Petković, R. Vasilić, N. Konjević, Investigation of plasma electrolytic oxidation on valve metals by means of molecular spectroscopy – a review, RSC Adv. 4 (2014) 25759–25789.
[40] S. Stojadinović, M. Perić, J. Radić-Perić, R. Vasilić, M. Petković, L. Zeković, Luminescence of the $B^1\Sigma^+$–$X^1\Sigma^+$ band system of MgO during plasma electrolytic oxidation of magnesium alloy, Surf. Coat. Technol. 206 (2012) 2905–2913.
[41] C.S. Dunleavy, J.A. Curran, T.W. Clyne, Time dependent statistics of plasma discharge parameters during bulk AC plasma electrolytic oxidation of aluminium, Appl. Surf. Sci. 268 (2013) 397–409.
[42] C.S. Dunleavy, I.O. Golosnoy, J.A. Curran, T.W. Clyne, Characterisation of discharge events during plasma electrolytic oxidation, Surf. Coat. Technol. 203 (2009) 3410–3419.
[43] C.S. Dunleavy, J.A. Curran, T.W. Clyne, Self-similar scaling of discharge events through PEO coatings on aluminium, Surf. Coat. Technol. 206 (2011) 1051–1061.
[44] A. Nomine, S.C. Troughton, A.V. Nomine, G. Henrion, T.W. Clyne, High speed video evidence for localised discharge cascades during plasma electrolytic oxidation, Surf. Coat. Technol. 269 (2015) 125–130.
[45] S.C. Troughton, A. Nomine, A.V. Nomine, G. Henrion, T.W. Clyne, Synchronised electrical monitoring and high speed video of bubble growth associated with individual discharges during plasma electrolytic oxidation, Appl. Surf. Sci. 359 (2015) 405–411.
[46] S.C. Troughton, A. Nomine, J. Dean, T.W. Clyne, Effect of individual discharge cascades on the microstructure of plasma electrolytic oxidation coatings, Appl. Surf. Sci. 389 (2016) 260–269.
[47] I.A. Aksey, J.A. Pask, Stable and metastable equilibria in the system SiO_2-Al_2O_3, J. Am. Ceram. Soc. 58 (1975) 507–512.
[48] S.H. Risbud, J.A. Pask, Mullite crystallization from SiO_2-Al_2O_3 melts, J. Am. Ceram. Soc. 61 (1978) 63–67.
[49] W.M. Kriven, J.A. Pask, Solid solution range and microstructures of melt-grown mullite, J. Am. Ceram. Soc. 66 (1983) 649–654.
[50] T. Takamori, R. Roy, Rapid crystalliszation of SiO_2-Al_2O_3 glasses, J. Am. Ceram. Soc. 56 (1973) 639–644.
[51] Y.M. Chiang, W.D. Kingery, Spinodal decomposition in a K_2O-Al_2O_3-CaO-SiO_2 glass, J. Am. Ceram. Soc. 66 (1983) C171–C172.
[52] R. Rossin, J. Bersan, G. Urbain, Viscosité de la silice fondue et de laitiers liquides appartenant au système SiO_2–Al_2O_3, CR Acad. Sci. Paris 258 (1964) 562–564.
[53] M.D. Klapkiv, Simulation of synthesis of oxide-ceramic coatings in discharge channels of a metal-electrolyte system, Mater. Sci. 35 (1999) 279–283.